# UNIVERSITY OF AMSTERDAM

## UvA-DARE (Digital Academic Repository)

### Emission and Transport of Light in Photonic Crystals

Koenderink, A.F.

**Publication date**
2003

**Citation for published version (APA):**
Koenderink, A. F. (2003). *Emission and Transport of Light in Photonic Crystals*. [, Universiteit van Amsterdam]. PrintPartners Ipskamp.

# Chapter 7

# Angular Redistribution of Diffuse Light

*Unavoidable structural disorder in photonic crystals causes weak multiple scattering of light. The consequences are extinction of incident and diffracted beams and the generation of diffuse light. We have studied the spectral and angular properties of the diffuse intensity transmitted by photonic crystals. The diffuse transmitted intensity is distributed over exit directions in a strikingly non-Lambertian manner, depending strongly on frequency. The remarkable frequency and angle dependence is quantitatively explained by a model incorporating diffusion theory and band structure on equal footing. The diffuse transmission reveals both the photonic band structure and the frequency-dependent extrapolation length. The model also describes the angle-dependent modification observed in emission spectra of internal sources in photonic crystals (Chapter 3). Total transmission corrected for the internal reflections shows a decrease of the transport mean free path slower than the characteristic Rayleigh law for frequencies in the range of first order Bragg diffraction. Hence the effect of structural disorder on the prospective higher order photonic band gap may be less severe than expected from previous reports.*

## 7.1 Introduction

As interference is at the basis of photonic crystal properties, any mechanism that destroys the coherence of the composite structure may be detrimental to the advances promised in recent literature [1, 2]. Calculations have recently shown the effects of fluctuations in size and position of the unit cell building blocks on the photonic band gap. A fluctuation of order ~ 5% of the unit cell size was found to be critical [3–5] in closing the band gap for inverse opals. Real two and three-dimensional structures inevitably suffer from disorder due to size-polydispersity, roughness and misarrangements of the building blocks. Fluctuations in size and position in current state of the art structures range from ~ 3.5% of the nearest neighbor distance for air spheres in inverse opals [6], to 4–7% for 2D semiconductor photonic crystal slabs [7, 8] and layer-by-layer woodpile crystals [9]. In experiments these faults result in, *e.g.*, reduced Bragg reflection efficiency [10], apparent broadening of pho-

127

tonic stop gaps [11], and large transmission losses through crystals and incorporated wave guides [2]. It remains unclear how to quantify structural disorder of fabricated structures. No satisfactory theoretical framework exists to relate structural disorder to its optical effect, which is gauged by the mean free path $\ell$ over which light becomes diffuse. Furthermore, the fate of randomly scattered photons is unknown after they leave the incoming Bloch wave, both from a theoretical and experimental point of view. Since absorption ideally does not occur, the diffuse energy density is expected to exceed the energy density of the incoming beam over most or all of the bulk of any three-dimensional photonic crystal that is larger in size than $\ell$ in all three dimensions. Hence, it is of prime importance to know where scattered photons go after a mean free path, and how they leave a photonic crystal.

Small angle X-ray scattering [6] and electron microscopy have provided a quantitative measure of structural disorder in terms of polydispersity and misarrangements of the components that build up the titania inverse opals. These parameters determine the transport mean free path $\ell$, which was recently determined experimentally for opals [12–14, see also Chapter 6] and inverse opals [13]. In this chapter we quantitatively account for the angle and frequency resolved characteristics of diffuse light transmitted by inverse opals. We show that the diffuse light is strongly affected by internal Bragg reflection, causing a drastic frequency-dependent redistribution of diffuse light over exit angles. This redistribution may be quantitatively explained by combining diffusion theory with internal reflections resulting from stop gaps in the photonic band structure. Our experiment also reveals the frequency dependence of the transport mean free path in the frequency range of the first order pseudo-gap. We find an increase of the scattering strength slower than Rayleigh's $\omega^4$ law with frequency. This observation is similar to the results for opals reported in Chapter 6. The scaling points at the dominance of polydispersity, small displacements and roughness as sources of random scattering [13], as opposed to missing spheres or grain boundaries [12].

## 7.2 Diffusion theory of angle-resolved transmission

When a light beam with an intensity spectrum $I_\omega^{in}$ is incident on a photonic crystal surface, some fraction $R_{\omega,\gamma}^{front} I_\omega^{in}$ is (Bragg) reflected. The dependence on frequency $\omega$ and incidence angle $\gamma$ (see Fig. 7.1) is indicated by subscripts, since these parameters are essential in the experiment, but not important in developing diffusion theory. The remaining light that is not Bragg reflected propagates into the sample where it suffers from extinction due to scattering by defects. The light removed from the incident beam is multiply scattered on length scales [15] equal to the transport mean free path $\ell$, which we have determined to be of the order of $\ell \approx 15\,\mu$m for our opals and inverse opals, as obtained from enhanced backscattering measurements presented in Chapter 6. Since the thickness $L$ of our crystals typically exceeds the mean free path, these crystals are opaque due to multiple scattering. In random media, the transport of multiply scattered light is usually well accounted for by the diffusion equation [15, 16]

introduced in Section 6.2. In this section, we review aspects of diffusion theory that are relevant for the angle-resolved transmission experiment presented in this chapter.

The success of diffusion theory depends on the use of appropriate boundary conditions, obtained by considering the diffuse fluxes at the sample walls. These conditions require that the diffuse intensity extrapolates to 0 at a distance $z_{e,\omega}$ from the sample walls, where the extrapolation length

$$z_{e,\omega} = \frac{2}{3}\left(\frac{1 + \bar{R}_{\omega}^D}{1 - \bar{R}_{\omega}^D}\right)\ell_{\omega}, \tag{7.1}$$

is determined by the polarization and angle-averaged internal reflectivity $\bar{R}_{\omega}^D$ of the sample boundaries [17–19]. The extrapolation length is crucial in correctly determining $\ell$ from enhanced backscattering or total transmission measurements, in which transmitted light integrated over all angles is collected. For example, it is well known that the total transmitted intensity $I_{\omega,\gamma}^T$ depends on the sample thickness according to

$$
\begin{aligned}
I_{\omega,\gamma}^T &:= I_{\omega}^{\text{in}} T_{\omega,\gamma} \\
&= I_{\omega}^{\text{in}}[1 - R_{\omega,\gamma}^{\text{front}}]\frac{\ell_{\omega} + z_{e,\omega}}{L + 2z_{e,\omega}}.
\end{aligned}
\tag{7.2}
$$

Unless $z_{e,\omega}$ is accurately known, $\ell_{\omega}$ can only be determined from the total diffuse transmission $T_{\omega,\gamma}$ if a series of measurements with fixed $R_{\omega,\gamma}^{\text{front}}$ is performed as a function of sample thickness $L$. For photonic crystals, varying $L$ is a challenge, hence the extrapolation length should be known for a total transmission measurement to be useful in determining $\ell_{\omega}$.

The extrapolation length ratio $\tau_{e,\omega} := z_{e,\omega}/\ell_{\omega}$ can be determined from angle-resolved diffuse transmission (see Fig. 7.1(a)), which is determined by refraction and reflection of the diffuse flux at the sample interface. The relation between the angle-dependent and the angle-averaged internal-reflection coefficient, and the use of diffuse transmission to study both, was first discussed by Zhu, Pine and Weitz [18]. Their argument is based on a simple flux consideration. Following their approach, we consider a semi-infinite diffusively scattering sample bounded by a plane interface. We assume the sample to be limited to $z > 0$, where the $z$-axis is the sample surface normal. One may consider the flux through a small surface d$s$ at the origin that is due to the diffuse energy density $W_{\omega,\gamma}(r, \phi, \alpha)$ in a volume element d$V = r^2 \sin\alpha\, dr d\phi d\alpha$ centered around a point $(r, \phi, \alpha)$, in spherical coordinates (see Fig. 7.1(b)). This flux d$J_{\omega,\gamma}$ d$s$ is set by the energy $W_{\omega,\gamma}(r, \phi, \alpha)$d$V$ contained in the volume element d$V$, the subtended fractional solid angle $\cos\alpha\, ds/4\pi r^2$, and the loss $\exp(-r/\ell_{\omega})$ due to scattering *en route* to d$s$:

$$dJ_{\omega,\gamma}ds = \frac{v_E}{\ell_{\omega}} \times W_{\omega,\gamma}(r, \phi, \alpha)dV \times \frac{\cos\alpha\, ds}{4\pi r^2} \times \exp(-r/\ell_{\omega}). \tag{7.3}$$

The ratio of energy velocity $v_E$ and $\ell_{\omega}$ is the inverse transport mean free time associated with the diffusion. The total flux from inside the sample onto the surface per
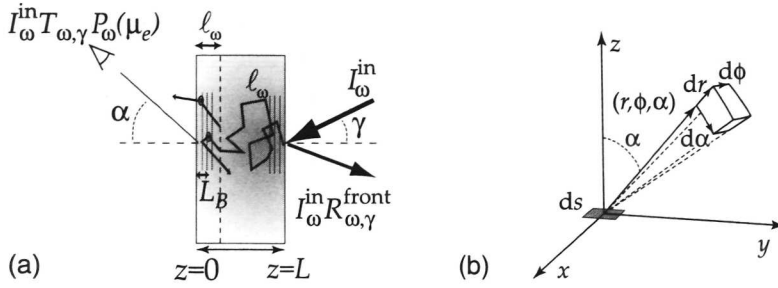
**FIGURE 7.1:** *(a) We consider a light beam $I^{in}_\omega$ incident on a photonic crystal sample. Generally, a fraction $R^{front}_{\omega,\gamma} I^{in}_\omega$ of the intensity is reflected, which depends on the frequency $\omega$ and the angle of incidence $\gamma$. In the sample the light diffuses with typical step length $\ell_\omega$. The diffuse glow on the transmission side is measured as a function of $\cos\alpha = \mu_e$. The depth of stop bands in the escape function is determined by $\ell$ and the Bragg attenuation length $L_B$ (see Section 7.5). (b) Coordinates used to calculate the contribution of a differential scattering volume $dV = r^2 \sin(\alpha) dr d\phi d\alpha$ inside a scattering sample to the diffuse flux through a surface $ds$. The z-axis is the inward normal to the sample interface.*

unit area may be found by integrating $dJ_{\omega,\gamma}$ over the upper half space

$$\mathcal{J}^{interior}_{\omega,\gamma} = \frac{v_E}{4\pi\ell_\omega} \int_0^\infty dr \int_0^{2\pi} d\phi \int_0^{\pi/2} d\alpha \; W_{\omega,\gamma}(r,\phi,\alpha) \exp(-r/\ell_\omega) \sin\alpha \cos\alpha.$$

(7.4)

It is important to note that the dominant contribution to the integral comes from the first mean free path ($z \lesssim \ell$) due to the exponential term. Secondly, as $W$ satisfies the diffusion equation it varies only slowly on length scales comparable to $\ell$. One may therefore replace $W_{\omega,\gamma}$ by a first-order Taylor expansion, to find the angle-dependent incident flux

$$J^{interior}_{\omega,\gamma}(\alpha) = \frac{v_E}{2} W_{\omega,\gamma}(z) \cos\alpha \sin\alpha + \frac{v_E \ell_\omega}{2} \frac{\partial W_{\omega,\gamma}(z)}{\partial z} \cos^2\alpha \sin\alpha \qquad \text{at } z = 0$$

(7.5)

after integration over $r$ and $\phi$ only. The total flux $\mathcal{J}^{interior}_{\omega,\gamma}$ is obtained by integrating $J^{interior}_{\omega,\gamma}(\alpha)$ over $\alpha$,

$$\mathcal{J}^{interior}_{\omega,\gamma} = \frac{v_E}{4} W_{\omega,\gamma}(z) + \frac{v_E \ell_\omega}{6} \frac{\partial W_{\omega,\gamma}(z)}{\partial z} \qquad \text{at } z = 0.$$

(7.6)

According to the same reasoning, the total flux $\mathcal{J}^{exterior}_{\omega,\gamma}$ due to the (virtual) diffuse intensity outside the sample reads

$$\mathcal{J}^{exterior}_{\omega,\gamma} = \frac{v_E}{4} W_{\omega,\gamma}(z) - \frac{v_E \ell_\omega}{6} \frac{\partial W_{\omega,\gamma}(z)}{\partial z} \qquad \text{at } z = 0.$$

(7.7)

This flux of photons entering the random medium from outside is expected to be identically zero, unless photons originating from inside the sample are reinjected due to internal reflection. Accordingly, one is led to define the angle-averaged reflection coefficient $\bar{R}_\omega^D$

$$\mathcal{J}_{\omega,\gamma}^{\text{exterior}} = \bar{R}_\omega^D \mathcal{J}_{\omega,\gamma}^{\text{interior}}, \tag{7.8}$$

which sets the extrapolative boundary condition

$$W_{\omega,\gamma}(z) - \frac{2}{3}\ell_\omega \frac{1 + \bar{R}_\omega^D}{1 - \bar{R}_\omega^D} \frac{\partial W_{\omega,\gamma}}{\partial z} = 0 \qquad \text{at } z = 0 \tag{7.9}$$

in agreement with the extrapolation length defined in Eq. (7.1). On the other hand, it stands to reason that the total flux $\mathcal{J}_{\omega,\gamma}^{\text{exterior}}$ reinjected into the sample, is obtained by summing the angle-dependent reflected flux $R_\omega^D(\alpha)J_{\omega,\gamma}^{\text{interior}}(\alpha)$ over all angles $\alpha$. This allows us to relate the angle-averaged diffuse-reflection coefficient $\bar{R}_\omega^D$ to the angle-dependent internal-reflection coefficient $R_\omega^D(\alpha)$. Summing over $\alpha$ one finds

$$\mathcal{J}_{\omega,\gamma}^{\text{exterior}} = \int_0^{\pi/2} R_\omega^D(\alpha) J_{\omega,\gamma}^{\text{interior}}(\alpha) d\alpha \tag{7.10}$$

$$= \frac{v_E}{2} C_{1,\omega} W_{\omega,\gamma}(z) + \frac{v_E \ell_\omega}{2} C_{2,\omega} \frac{\partial W_{\omega,\gamma}}{\partial z} \qquad \text{at } z = 0,$$

$$\text{with} \quad C_{n,\omega} = \int_0^{\pi/2} R_\omega^D(\alpha) \cos^n(\alpha) \sin\alpha \, d\alpha. \tag{7.11}$$

Identifying $\mathcal{J}_{\omega,\gamma}^{\text{exterior}}$ in Eq. (7.10) with $\bar{R}_\omega^D \mathcal{J}_{\omega,\gamma}^{\text{interior}}$ according to (7.8), one may solve for $\bar{R}_\omega^D$ to obtain

$$\bar{R}_\omega^D = \frac{3C_{2,\omega} + 2C_{1,\omega}}{3C_{2,\omega} - 2C_{1,\omega} + 2}. \tag{7.12}$$

This appears to be the key expression to relate the angle-dependent internal-reflection coefficient $R_\omega^D(\alpha)$ to the angle-averaged reflection coefficient $\bar{R}_\omega^D$, and to the extrapolation length ratio $\tau_{e,\omega}$ through Eq. (7.1).

Angle-resolved diffuse transmission experiments are very useful to determine the extrapolation length, as well as obtain information about the angle-dependent internal-reflection coefficient $R_\omega^D(\alpha)$. Only the fraction $J_{\omega,\gamma}^{\text{interior}}(\alpha)[1 - R_\omega^D(\alpha)]$ of the flux incident from inside the sample onto the sample boundary is transmitted, as the remaining fraction $J_{\omega,\gamma}^{\text{interior}}(\alpha)R_\omega^D(\alpha)$ contributes to the reentrant flux. Using the expression (7.5) for $J_{\omega,\gamma}^{\text{interior}}(\alpha)$, and the boundary condition $W_{\omega,\gamma}(z) = z_{e,\omega}\partial_z W_{\omega,\gamma}(z)$, one finds that the intensity transmitted between angles $\alpha$ and $\alpha + d\alpha$ equals

$$I_{\omega,\gamma}(\alpha)d\alpha = \frac{v_E}{2} \frac{\partial W_{\omega,\gamma}}{\partial z} \cos\alpha \, [z_{e,\omega} + \ell_\omega \cos\alpha] \cdot [1 - R_\omega^D(\alpha)] \sin\alpha \, d\alpha \quad \text{at } z = 0. \tag{7.13}$$

The angle-resolved diffuse transmitted intensity can be factorized

$$I_{\omega,\gamma}(\mu_e)\mathrm{d}\mu_e = I_\omega^{\text{in}} T_{\omega,\gamma} P_\omega(\mu_e)\mathrm{d}\mu_e \tag{7.14}$$

into the total transmission $T_{\omega,\gamma}$ and the probability $P_\omega(\mu_e)\mathrm{d}\mu_e$ for a diffuse photon in the sample to be transmitted at an angle between $\alpha = \cos^{-1}\mu_e$ and $\cos^{-1}(\mu_e + \mathrm{d}\mu_e)$. The total transmitted intensity

$$I_{\omega,\gamma}^T = I_\omega^{\text{in}} T_{\omega,\gamma} = \frac{1}{3}v_E\ell\frac{\partial W_{\omega,\gamma}(z)}{\partial z} = D\frac{\partial W_{\omega,\gamma}(z)}{\partial z} \quad \text{at the exit interface} \tag{7.15}$$

equals the flux through the sample interface given by Fick's law. The normalized probability distribution $P_\omega(\mu_e)$ is given by

$$P_\omega(\mu_e) = \frac{3}{2}\mu_e[\tau_{e,\omega} + \mu_i] \cdot [1 - R_\omega^D(\mu_i)]. \tag{7.16}$$

As $P_\omega(\mu_e)$ describes the distribution of photons over the available escape angles, it will be referred to as 'escape function'. One should be aware that we have slipped in a distinction between internal angle $\cos^{-1}\mu_i$, and external angle $\cos^{-1}\mu_e$ relative to the z-axis into Eq. (7.16), which accounts for refraction effects at the interface.

The angular dependence of the escape function $P_\omega(\mu_e)$ has been found to agree with experiments on random media if an effective refractive index is used to model $R_\omega^D(\mu_i)$ according to Fresnel's law, and to convert internal to external propagation angles $\cos^{-1}\mu_i$ resp. $\cos^{-1}\mu_e$ using Snell's law [18, 19]. As the refractive indices of constituents of usual random media such as powders or macroporous sponges are barely frequency dependent [20–22], only a weak frequency dependence of $T$, $P$ and $\ell$ would be expected. For highly dispersive photonic crystals, however, the Fresnel model is not expected to describe the internal-reflection coefficient well at all. In contrast, light emanating from a depth $z < \ell$ from the crystal surface is expected to be Bragg attenuated (i.e., internally reflected) for angles and frequencies matching the Bragg condition [23, 24]. Hence the photonic band structure is expected to give rise to a strongly angle and frequency-dependent internal-reflection coefficient $R_\omega^D(\mu_i)$, resulting in stop bands in the diffuse transmission. Furthermore, these stop bands cause a frequency-dependent extrapolation length [13], as witnessed by the experiment presented in Chapter 6.

It is clear that the mean free path $\ell$ in photonic crystals can only be quantitatively obtained from enhanced backscattering or total transmission if the frequency-dependence of the extrapolation length is taken into account. A reduction of the enhanced backscattering cone width due to enhanced internal reflection has indeed been observed for frequencies matching the first Bragg diffraction order of an inverse opal photonic crystal [13, see Chapter 6]. Furthermore, we note that the refraction law to convert $\mu_i$ to $\mu_e$ is highly complex in photonic crystals [25]. In comparing external reflectivity measurements with band structure calculations, reasonable agreement has been obtained for the lowest order stop bands using Snell's law with a geometrically averaged refractive index [26, 27].

In this chapter we report experimentally determined escape functions $P_\omega(\mu_e)$ of inverse opals. We discuss the measured frequency-dependence of the escape function at chosen detector angles (Section 7.4.1) in terms of photonic stop gaps. In Section 7.4.2 a different perspective is offered by considering the angular redistribution of diffuse light, *i.e.*, the angle-dependence of the escape function for several chosen frequencies. We combine the diffusion theory with a simple model for the angle and frequency dependence of the internal-reflection coefficient $R_\omega^D(\mu_i)$ in Section 7.5. Subsequently, we discuss the agreement between the model and the experimental data over the full angular and frequency range, and address the magnitude of the internal-reflection coefficient. In Section 7.7, we present the total transmission measurements, and we use the extrapolation length ratio determined from Section 7.5 to interpret the total transmission measurements in terms of the transport mean free path.

## 7.3 Experiment

We have studied *fcc* photonic crystals consisting of air spheres in anatase TiO$_2$ (refractive index $2.7 \pm 0.4$) with lattice parameters $a = 800, 900, 930 \pm 20$ nm. Details of fabrication and characterization are reported in Ref. [6]. The surfaces of the samples are parallel to the 111 crystal planes. These photonic crystals are strongly photonic, as they have a relative frequency width of the lowest order Bragg diffraction, or L-gap, equal to $\Psi = 0.12$. The crystals studied in this chapter have larger lattice spacing than the crystals discussed in Chapters 3, 4 and 6 (see Fig. 3.3), but are otherwise similar. The colorful opalescence, corresponding to higher diffraction orders, indicates good sample quality. Most of the structural disorder is inherited from the opal templates. As probed by small angle X-ray scattering [6], the polydispersity and rms displacements of the air spheres from the lattice sites are less than 3% of the nearest neighbor distance throughout the bulk of the crystals. Together with the roughness of the titania shells ($\leq 10$ nm [6]) this constitutes the main source of scattering determining the transport mean free path of $\ell \sim 15 \, \mu$m [13, Chapter 6]. As the thickness $L \sim 200 \, \mu$m of the samples exceeds the mean free path, diffuse transport of light is indeed expected. Samples were mounted on a rotation stage to allow control over the orientation of the surface normal (parallel to the 111 reciprocal lattice vector) relative to the incident beam. As shown in Figure 7.2 the detector was mounted on a separate concentric rotation stage, allowing the detector angle $\alpha$ relative to the sample surface normal to be varied from 0 to 90 degrees, independently of the incidence angle $\gamma$.

Diffuse-transmission spectra were recorded in the range $0° \leq \alpha \leq 90°$ every $5°$. For spectrally resolved measurements, light from an incandescent lamp (tungsten-halogen) was passed through a Fourier-Transform spectrometer (Biorad FTS-6000) operated at a resolution of 32 cm$^{-1}$. The beam emanating from the spectrometer was focused onto a pinhole, acting as a point source. This point source was imaged with a camera objective (f=50 mm) onto a spot of 0.40 mm radius encompassing many domains on the sample surface. The apex angle of the incident beam ($10°$) was chosen to optimize the incident power. The angular resolution for diffuse transmission is set by
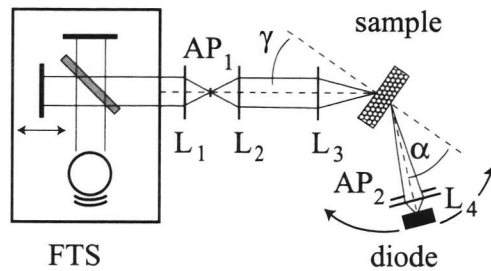
FIGURE 7.2: *Overview of the diffuse-transmission setup. The output of a tungsten-halogen source is passed through a Fourier-Transform Spectrometer (FTS). The beam is focused onto a pinhole $AP_1$ using lens $L_1$. The pinhole acts as a point source which is imaged on the front sample surface using lens $L_2$ and camera objective $L_3$. The angle of incidence $\gamma$ is controlled by rotating the sample. The detector angle $\alpha$ is changed independently by rotating the diode together with aperture $AP_2$ and lens $L_4$ which determine the angular acceptance.*

the aperture of the detector of 5°, and is independent of the apex angle of the incident beam. Angle-resolved measurements of the diffuse transmitted intensity were obtained in the frequency range from 5500 to 14000 cm$^{-1}$ by using both Si and InGaAs photodiodes. Higher frequencies can only be probed by replacing the light source. The diode signal yields an interferogram which is Fourier transformed to determine the diffuse transmitted intensity $I_{\omega,\gamma}(\mu_e = \cos\alpha)$ defined in Eq. (7.14). The total transmitted intensity spectra $I_{\omega,\gamma}^T$ are determined by summing the angle-resolved spectra of diffuse transmitted intensity weighted by $2\pi\sin\alpha\,d\alpha$ to approximate the integration over $2\pi$ solid angle. The total transmission $T_{\omega,\gamma}$ (Eq. (7.2)) is obtained by normalizing the total transmitted intensity spectrum $I_{\omega,\gamma}^T$ to the lamp spectrum $I_\omega^{\text{in}}$, measured by removing the sample from the setup. The escape functions $P_\omega(\mu_e = \cos\alpha)$ are determined by dividing the angle-resolved spectra $I_{\omega,\gamma}(\mu_e)$ of diffuse transmitted intensity by the total transmitted intensity spectrum $I_{\omega,\gamma}^T$, as expressed by Eq. (7.14). Thus, the escape functions are independent of the lamp spectrum.

Alternatively, a HeNe ($\lambda = 632$ nm) or Nd:YVO$_4$ ($\lambda = 1064$ nm) laser beam could be used as single-frequency probes of the diffuse transmission, using a chopper and lock-in amplifier. The laser beam, not shown in Figure 7.2, overlapped with the white light beam starting from lens $L_1$. The greater sensitivity allowed the use of cross-polarized detection, contrary to the white light experiments. Cross-polarized detection avoids contributions of the unscattered beam to the detected signal.

## 7.4  Escape functions

Several raw spectra $I_{\omega,\gamma}(\mu_e)$ are shown in Figure 7.3 that demonstrate the diffuse transmitted intensity at chosen angles $\alpha = \cos^{-1}\mu_e = 15°$, 30°, 50°, 75°, recorded for incidence angle $\gamma = 0°$. These data were obtained from a sample with lattice spacing $a = 930$ nm and recorded using an InGaAs detector. Comparison with the lamp
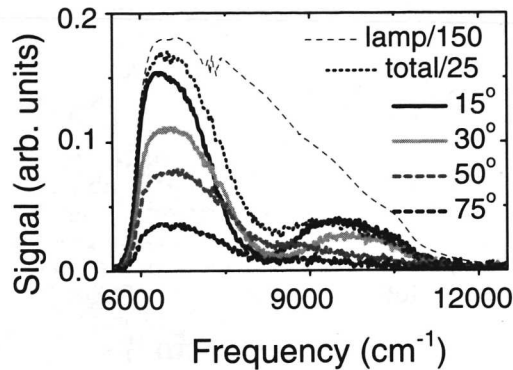
FIGURE 7.3: *Raw spectra of diffuse light transmitted by a titania inverse opal with a = 930 nm, for detection angles α = 15, 30, 50 and 75°, and incidence angle γ = 0°. The spectrum of the lamp as recorded by the same InGaAs diode, as well as the total transmitted intensity spectrum are also shown (scaled as indicated). The detector acceptance angle, which affects the scaling factor between raw spectra and total transmission spectrum, was 5°.*

spectrum reveals several striking features. Firstly, for low frequencies $\sim 6000$ cm$^{-1}$ we observe a steady decrease in intensity with increasing angle, as would be expected from the dominant $\cos \alpha$ proportionality in Eq. (7.16). For higher frequencies, the lineshapes appear to depend on the detection angle $\alpha$. Compared to the lamp spectrum, a wide stop band appears, centered at 8100 cm$^{-1}$ for $\alpha = 15°$. To a large degree this attenuation band remains at the same frequency when the detector angle is increased. The total transmitted intensity spectrum $I^T_{\omega,\gamma}$ (dotted curve) indeed shows a wide attenuation band at 8000 cm$^{-1}$. The total transmission $T_{\omega,\gamma}$ will be discussed in Section 7.7. Closer examination of the angle resolved spectra shows that spectra at increased detection angle are further attenuated in a band shifting to larger frequency with increasing detector angle $\alpha$, compared to the $\alpha = 15°$ spectrum. This dependence of $\alpha$ is best studied by examining the escape function.

### 7.4.1 Escape function versus frequency at selected angles

Escape functions $P_\omega(\mu_e)$ at detector angles $\alpha = \cos^{-1} \mu_e = 15°, 25°, 35°, 45°, 55°, 65°, 75°$ for an inverse opal with lattice parameter $a = 930$ nm are shown as a function of frequency $\omega$ in Figure 7.4. These data belong to the same set as the raw spectra in Fig. 7.3, and were obtained by dividing by the total transmitted intensity spectrum and correcting for the angular aperture d $(\cos \alpha)$. The frequency range was extended by combining the dataset represented in Fig. 7.3 with complementary data obtained by replacing the InGaAs diode with a Si detector (used for $\omega \geq 10500$ cm$^{-1}$) . In the common frequency window from 9000 to 11500 cm$^{-1}$ in which both detectors are sensitive, the escape functions matched seamlessly within the noise for all detector angles $\alpha$. It should be noted that no scaling constants are involved in Figure 7.4.
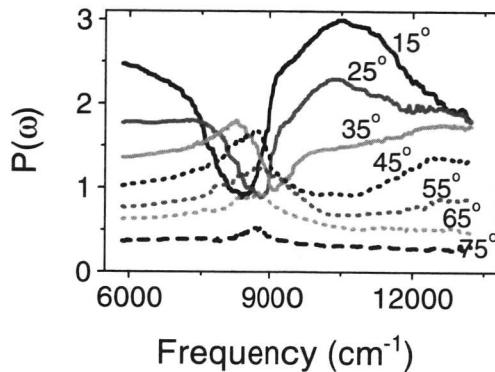
FIGURE 7.4: *Photon escape function as a function of frequency for an inverse opal with lattice parameter a = 930 nm for exit angles α = 15°, 25°, 35°, 45°, 55°, 65°, 75°. The incidence angle is γ = 0°. The top axis shows normalized frequency units a/λ where λ is the wavelength in vacuum. No relative scaling or offset was applied to the curves.*

We do not find a dependence of the escape function on the incidence angle $\gamma$ for $0° \leq \gamma \leq 30°$. This result validates the factorization in Eq. (7.14), as it confirms that $P_\omega(\mu_e) = I_{\omega,\gamma}(\mu_e)/I_{\omega,\gamma}^T$ is independent of $\gamma$. The factorization may be understood from the diffusive nature of the samples; as the direction of propagation is fully randomized, the probability for a photon to leave the sample at a specific exit angle $\alpha$ is not dependent on the incidence geometry. The only effect of the incidence angle $\gamma$ is expected to be due to the reflectivity of the front surface ($R_\gamma^{front}(\omega)$ in Eq. (7.2)), which reduces the *total* transmission $T_{\omega,\gamma}$ for frequencies and incident angles matching the Bragg condition.

At low frequencies $\lesssim 6700$ cm$^{-1}$ the escape function is unaffected by internal reflection and typical for a random medium with $z_e \approx \frac{2}{3}\ell$. As is evident in Fig. 7.4, the escape function at an exit angle of $\alpha = 15°$ is significantly reduced by $\gtrsim 70\%$ in a stop band centered at $\sim 8200$ cm$^{-1}$ with full width at half maximum (FWHM) $\sim 1300$ cm$^{-1}$. This stop band in the escape function occurs due to internal Bragg reflections, as captured in the term $[1 - R_\omega^D(\mu)]$ in Eq. (7.16), and moves to higher frequencies with increasing exit angle $\alpha$. At angles $\alpha$ exceeding $\sim 40°$, a much wider gap from 9000 to 12000 cm$^{-1}$ is evident in Figure 7.4. Similar broadening, and the occurrence of a double-peak structure has been observed in reflectivity experiments [27, 28] and luminescence experiments (Chapter 3), and has been explained in terms of a multiple-Bragg wave coupling involving both 111 and 200 reciprocal lattice vectors [27]. Figure 7.4 shows that the stop gap at these larger angles is preceded by a frequency range characterized by an *increase* of the escape function relative to the low frequency value. This frequency range is coincident with the stop band at small detector angles. The increase has the same origin as the enhanced escape probability in the frequency range 9000 – 12000 cm$^{-1}$ evident in the escape function spectrum at small detector angles. As escape directions within a stop gap are blocked by internal Bragg

reflection, photons are more likely to escape in the remaining directions, giving rise to an *enhanced* escape probability in directions *not coincident* with a stop gap. Equivalently, this enhanced escape probability is accounted for in the model (7.16) for $P_\omega(\mu)$ as an increase of the extrapolation length due to a larger average internal-reflection coefficient.

Similar results were obtained for a multitude of samples with different lattice parameters ($a = 800, 900, 930$ nm). The shift along the frequency-axis of the escape functions with lattice parameter confirms the photonic origin of the redistribution of the diffuse intensity (see Fig. 3.3). In conclusion, these observations clearly show that the diffuse intensity possesses a pronounced angle and frequency-dependent structure due to the strongly photonic crystal. This point is particularly important in the interpretation of common experiments, such as reflectivity or transmissivity measurements. The diffuse contribution to the signal may clearly not be corrected for by assuming a frequency independent background. In this respect a transmission measurement can be particularly misleading. Even if scattering by disorder precludes any coherent transmission (*i.e.*, for thick samples $L/\ell \gtrsim 5$), a detector along the incoming direction will still register a diffuse spectrum with an attenuation band coincident with the photonic stop gap. Evidently, a stop gap in transmission may only be trusted if the transmission for frequencies just *outside* the stop gap is close to 100%, indicative of low scattering. This requires an absolute calibration of the transmission. In the frequency range of higher order diffraction and the prospective photonic band gap, no strongly photonic crystals with thickness less than $\ell$ but larger than two unit cells appear to have been reported to date.

### 7.4.2 Strongly non-Lambertian redistribution

The redistribution of diffuse intensity over exit angles may be more fully appreciated by considering the escape function as a function of angle for selected constant frequencies, *cf.* Figure 7.5. The horizontal scale in terms of $\mu$ represents the large contribution of large exit angles in the distribution of intensity over the available hemisphere of exit directions. For clarity, the exit angle range from 0° to 45° covering half of the available polar exit angle range is indicated in gray. For reference we studied a calibration sample consisting of a vial with a dilute suspension of polystyrene spheres in water (dashed curve in Figure 7.5). In accordance with Ref. [19, 29], we find nearly Lambertian behavior corresponding to $P_L(\mu_e) = \frac{3}{2}\mu_e(\frac{2}{3} + \mu_e)$. Detailed analysis shows that the escape function of the calibration sample is accurately modelled by Eq. (7.16). A Fresnel-type model for the internal-reflection coefficient was used, assuming an effective index of 1.33 relevant for water, and taking multiple reflections in the vial walls into account [19].

For frequencies below the L-gap ($\omega = 6270$ cm$^{-1}$) the escape function of an inverse opal with $a = 930$ nm closely resembles the escape function measured for the random calibration sample, as witnessed by Fig. 7.5. From a fit of diffusion theory with a Fresnel model for the internal-reflection coefficient, we estimate an effective refractive index of $n_{eff} = 1.27 \pm 0.15$. This effective index is consistent with a 10 to
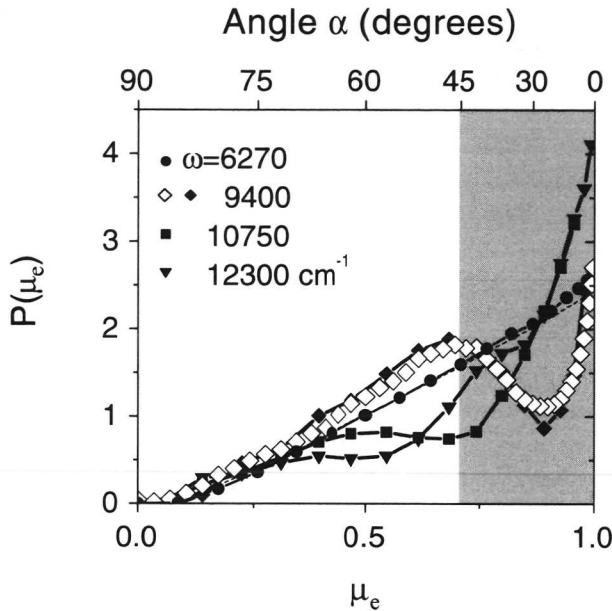
FIGURE 7.5: *Photon escape function as a function of the cosine $\mu_e$ of the escape angle $\alpha$ for an inverse opal with lattice parameter $a = 930$ nm for frequencies $\omega = 6270, 9400, 10750, 12300$ cm$^{-1}$ (solid circles, diamonds, squares, resp. triangles) as extracted from a white light data set. These frequencies correspond to $a/\lambda = 0.58, 0.87, 1.0$ and $1.14$. Open diamonds show a measurement obtained from the same sample using a Nd:YVO laser beam ($\omega = 9400$ cm$^{-1}$). For an angular scale, refer to the top axis. The shaded region corresponds to half the available range for the exit angle $\alpha$ relative to the surface normal. The dashed line partially obscured by closed circles corresponds to a calibration measurement on a dilute colloidal suspension.*

20% volume fraction of solid material, depending on whether the effective index is assumed to correspond to the volume averaged index or volume averaged dielectric constant. The nearly Lambertian distributions for low frequencies should be contrasted to the strongly non-Lambertian distributions observed for higher frequencies. As an example we discuss the angular distribution of emitted photons at a frequency of 9400 cm$^{-1}$, to the blue of the L-gap, shown in Figure 7.5. The escape function at this frequency is clearly reduced in the range from $\alpha = 10°$ to $40°$, and enhanced both for near-normal exit angles and for exit angles exceeding $40°$. These features, as extracted from the white-light experiment, are excellently reproduced in an additional single-frequency measurement using a Nd:YVO$_4$ laser beam ($\lambda = 1.064$ $\mu$m), also shown in Fig. 7.5. For increasing frequency ($\omega = 10750$, and $12300$ cm$^{-1}$) the angular range of suppression relative to the Lambertian distribution shifts to larger $\alpha$, leaving a central cone around the surface normal within which the escape probability is strongly enhanced by a factor up to $\sim 2$.
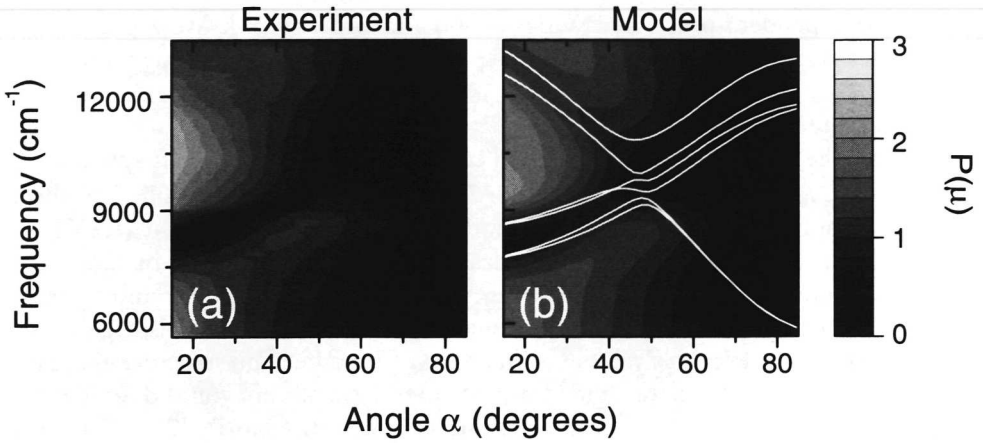
FIGURE 7.6: *(a) Contour plot of the measured photon escape function as a function of exit angle α and optical frequency corresponding to an inverse opal with a = 930 nm. (b) Contour plot of the fitted escape function, according to the diffusion model Eq. (7.16) combined with an internal-reflection coefficient derived from the band structure Eq. (7.17). The lowest 6 bands along the LU direction are plotted in white, using the effective index to transform internal propagation angles into external propagation angles. The band structure alone can not fully explain the frequency and angle dependence of the escape function. Features not expected from the band structure are, for instance, the enhanced escape probability for α < 30° and 9000 ≲ ω ≲ 12000 cm⁻¹, and for α > 30° and 7500 ≲ ω ≲ 9000 cm⁻¹. The common gray scale is displayed on the far right.*

## 7.5 Diffuse internal-reflection model

The full dataset to which Figure 7.4 corresponds is presented as a contour plot in Figure 7.6(a). For angles below ~ 40° the shift of the stop gap to higher frequency with increasing exit angle is clearly discerned, as well as the widening of the stop gap for larger exit angles due to multiple Bragg wave coupling [27]. The concomitant enhancement of the escape function is evident in the range 9000–12000 cm⁻¹ for small angles $\alpha < 30°$ and in the range 7500–9000 cm⁻¹ for large exit angles $30° < \alpha < 60°$. In this section we proceed with a quantitative description of the data in terms of a semi-empirical model that combines diffusion theory with a model derived from a band structure calculation for the internal-reflection coefficient $R_\omega^D(\mu)$.

### 7.5.1 Internal-reflection coefficient

The internal-reflection coefficient of the inverse opals is modelled as the sum of two Gaussian reflection peaks

$$R_\omega^D(\mu_i) = R_1(\mu_i) \exp\left[-\frac{(\omega - \omega_1(\mu_i))^2}{2\Delta\omega_1(\mu_i)^2}\right] + R_2(\mu_i) \exp\left[-\frac{(\omega - \omega_2(\mu_i))^2}{2\Delta\omega_2(\mu_i)^2}\right], \qquad (7.17)$$

139

with angle-dependent peak reflectivities $R_{1,2}(\mu)$ and widths $\Delta\omega_{1,2}$. We expect such a model to capture the essential frequency dependence of the multiple Bragg wave coupling [24, 27] if the center frequencies $\omega_{1,2}(\mu)$ are chosen consistent with the photonic band structure.

We use the band structure for a model consisting of close-packed air spheres (radius $r = \frac{1}{4}\sqrt{2}a$) on an *fcc* lattice surrounded by high-index ($\varepsilon = 6.5$) spherical shells with outer radius $1.09r$, connected by cylindrical windows of radius $0.4r$ (see Chapter 3). The window size and the volume fraction of solid material are in agreement with structural data [6], and the resulting band structure has been found to agree with reflectivity bands in both the frequency range of first and second Bragg diffraction order [27, 30]. Previously, it has been observed that the band structure along the LU-line in reciprocal space (extended outside the first Brillouin zone) describes the angle-dependent reflectivity of polycrystalline samples satisfactorily [27]. Therefore we have calculated the dispersion relation along the LU-line, and determined $\omega_1(\mu)$ and $\omega_2(\mu)$ from the calculated stop band edges. To convert internal to external propagation angle we have used Snell's law[1]. An average refractive index $n = 1.28$ was chosen, consistent with the volume averaged dielectric constant for a titania volume fraction of 11%.

Contrary to the fixed reflection band center frequencies $\omega_{1,2}(\mu)$, we have adjusted the reflection peak widths $\Delta\omega_{1,2}(\mu)$, and the reflection peak heights $R_{1,2}(\mu)$ to obtain an optimal fit of the diffusion model Eq. (7.16) with internal reflection Eq. (7.17) to the data. We expect the parameter functions $R_{1,2}(\mu)$ and $\Delta\omega_{1,2}$ to vary smoothly with angle, and approximate them using cubic polynomials in $\mu$. The polynomial coefficients are determined using a nonlinear least-squares minimization algorithm to optimally fit Eq. (7.16) to the data. In Section 7.5.2, we will discuss the agreement between the data and the simple model outlined above, and the angle dependence of the fitted lowest order peak reflectivity. In Section 7.7 we will review the frequency dependence of the extrapolation length ratio specified by the fitted $R_\omega^D(\mu)$ through Eq. (7.1).

### 7.5.2 Escape functions and band structure

In Figure 7.6(b) both the fit to the data in Fig. 7.6(a) and the lowest six calculated bands are displayed. The average difference between measured and calculated escape function is between 5 and 10%. The excellent correspondence of the model to the experimental data is more clearly displayed for two key frequencies in Figures 7.8(a) and (c). The agreement between the data and the model Eqs. (7.16, 7.17) is striking, given the simplicity of the model for the internal-reflection coefficient, the empirical nature of the escape function theory, and the limitations on the validity of diffusion theory imposed by the modest optical sample thickness ($2 < L/\ell < 10$).

---

[1] Refraction may be more accurately taken into account by using parallel momentum conservation at the interface. Within the theory of diffusion with internal reflections, the effective index will always remain a source of inconsistency, since it is unclear how to deal with the associated Fresnel reflections.
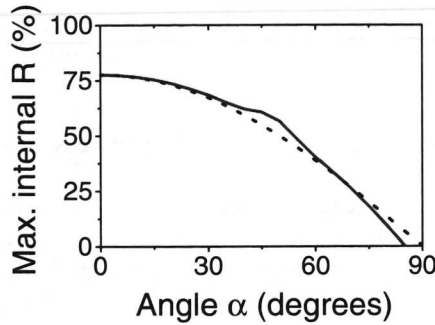
FIGURE 7.7: *Solid line: the fitted peak internal-reflection coefficient $R_\omega^D$ versus exit angle $\alpha$ for frequency $\omega$ coincident with the lowest order stop band center frequency $\omega_1(\cos\alpha)$. This curve corresponds to the fit (see Fig. 7.6(b)) to the experimental data shown in Fig. 7.4, 7.5 and 7.6(a). The peak internal-reflection coefficient decreases as $\cos(\alpha)$ (dashed line).*

Figure 7.6(b) clearly demonstrates that for quantitative understanding of the angle-resolved diffuse transmission, the band structure is useful but *not sufficient*. Although the lowest diffraction order at near-normal incidence in the band structure evidently corresponds to the attenuation band in the diffuse transmission, the enhanced transmission probability for wave vectors outside a stop band can not be explained from the dispersion relation alone. The extrapolation length ratio $\tau_e$ is the essential parameter determining the redistribution of intensity over exit directions. The frequency dependence of the extrapolation length ratio will be discussed in Section 7.7.

It is interesting to monitor the magnitude of the fitted internal-reflection coefficient of the lowest stop gap as a function of the photon escape angle $\alpha$. As shown in Figure 7.7 for the fit to the experimental data in Fig. 7.6(a), we find a decrease of the reflection coefficient of the lowest gap with increasing angle which follows a cosine behavior over a large angular range. This supports our earlier report [24] in Chapter 3, stating that the stop gap depth for $\alpha = 0°$ in luminescence spectra (*i.e.*, using an internal source of diffuse light) is determined by the ratio of Bragg attenuation length and the transport mean free path $\ell$. Briefly, diffuse photons emanating from a depth $z < \ell$ from the crystal-air interface propagate ballistically to the interface. Photons may be redirected into Bragg directions by scattering off defects in the surface layer $z < \ell$. Since $\ell$ is larger than the Bragg attenuation length $L_B \approx 0.2\ell$, light scattered at $z < L_B$ is hardly Bragg attenuated, while light scattered in $L_B < z < \ell$ results in a stop band (*cf.* Fig. 7.1). The stop band depth for $\alpha = 0°$ is therefore estimated as $1 - R_{\omega_c}^D(\alpha = 0) \sim 1 - L_B/\ell$, where $\omega_c$ is the stop band center frequency. This geometrical argument may be generalized by noting that for larger exit angles $\alpha$, the path length to the crystal air interface increases with $\cos\alpha$. This increases the probability of being scattered at $z < L_B$, and reduces the internal-reflection coefficient to $\sim L_B \cos\alpha/\ell$, in agreement with Fig. 7.7. We conclude that the mechanism of diffusion and internal

reflection proposed for the angular redistribution of fluorescence from sources inside strongly photonic crystals [24] is confirmed by the present results and analysis.

## 7.6    Diffusion in case of a band gap: beyond Kossel lines

The exemplary agreement between the diffusion model and the experimental data is more clearly shown for two key frequencies in Figure 7.8(a) and (c). For a frequency in the L-gap, $\omega = 8200$ cm$^{-1}$, both the data and the diffusion model of the escape function are strongly reduced relative to the Lambertian distribution $P_L$ in the range from $\alpha = 0$ to $35°$ (Fig. 7.8(a)). This range is shifted to larger angle in Fig. 7.8(c), corresponding to a frequency of 9300 cm$^{-1}$. If the diffuse intensity corresponding to the escape function profile for $\omega = 8200$ cm$^{-1}$ would be projected on a screen, one would find a dark disk concentric with the sample normal, with radius corresponding to $\alpha = 35°$. For $\alpha$ beyond $35°$ the intensity would be slightly in excess of $P_L$. For the frequency $\omega = 9300$ cm$^{-1}$ above the L-gap, one would rather find a dark ring, surrounding a bright disk. We illustrate these concepts, by considering stereographic plots of the photon excess distribution

$$\Delta P_\omega(\mu_e) = P_\omega(\mu_e) - P_L(\mu_e) \tag{7.18}$$

versus exit angle in Figure 7.8(b),(d). In the stereographic plots, a polar coordinate $(r, \phi)$ corresponds to an azimuthal exit angle $\phi$ and polar exit angle $\alpha$ such that $r(\alpha) = \sin\alpha/(\cos\alpha + 1)$. A measurement on single crystal samples would show an azimuthal dependence of the escape function, since the 200 family of reciprocal lattice vectors oblique to the sample surface is involved in the Bragg diffraction. This dependence is lost in our experiment due to polycrystalline averaging. Azimuthally independent grey scales in Fig. 7.8(b),(d) have been generated from the model function plotted in (a) and (c). The dark disk in Fig. 7.8(b), and the forbidden ring with inner radius $\alpha = 34°$ and outer radius $\alpha = 50°$ in (d) are reminiscent of Kossel lines. Dark Kossel lines in diffuse transmission have been reported for weakly photonic crystals [31, 32]. These lines should in fact be called Seemann lines, as they are solely due to internal Bragg diffraction of diffuse light, and do not involve the subtle intensity features occurring in the X-ray fluorescence lines discovered by Kossel [33, 34]. Despite the distinction, we will use the term Kossel lines to remain consistent with current practice in the field of photonic crystals. Weakly photonic colloidal single crystals cause narrow Kossel lines in diffuse transmission. In such cases, the nearly free-photon approximation can be used to determine the crystal symmetry and orientation based on the geometry of the dark circles and hyperbolas. For strongly photonic inverse opals, the dark areas are not necessarily circles or hyperbolas, and the width of the internal reflection lines is extraordinarily large. The dark rings evident in Figure 7.5 and 7.8 can extend over $\gtrsim 30\%$ of the $2\pi$ sr solid angle, and the geometry of the internal reflection is strongly affected by multiple Bragg wave coupling. A geometrical analysis [31, 32] of dark lines in diffuse transmission to obtain the crystal symmetry is therefore not viable, but the full band structure should be used for
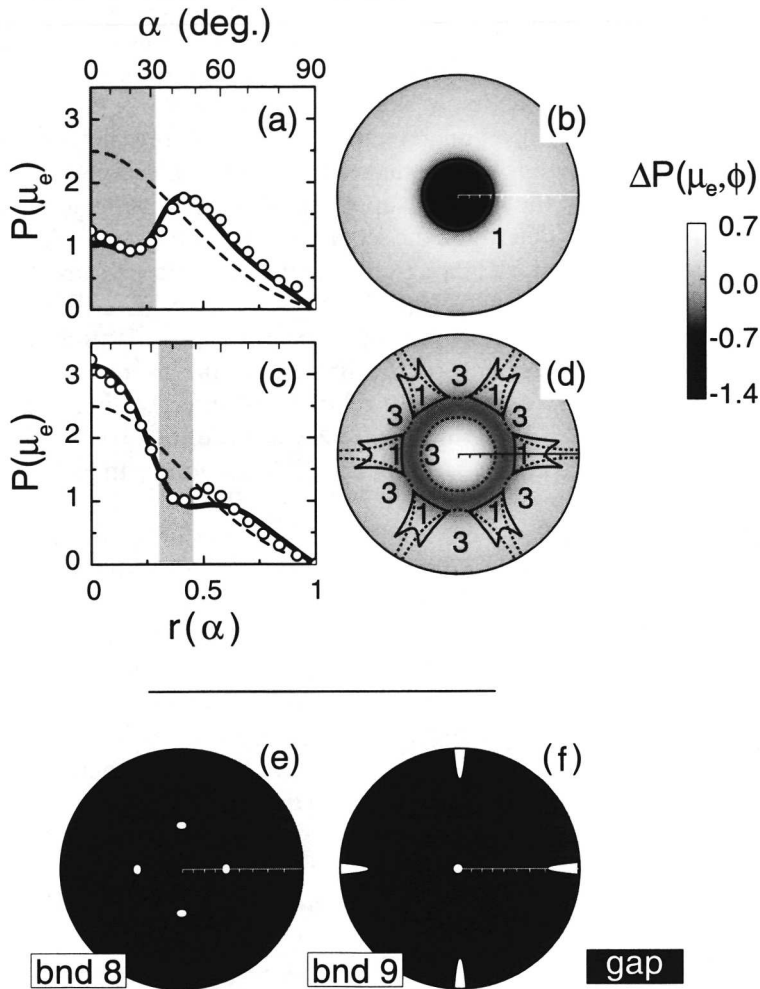
FIGURE 7.8: *Photon exit distribution $P(\mu_e)$ for frequencies $\omega = 8200$ cm$^{-1}$ (a), resp. 9300 cm$^{-1}$ (c) measured for an inverse opal with $a = 930$ nm. Both the data (dots) and the adapted diffusion model (solid curves in (a) and (c)) strongly differ from the Lambertian distribution $P_L$ (dashed curves). Grey areas indicate forbidden exit angles according to the dispersion surface analysis. (b) and (d): stereographic plots of the photon excess distribution $\Delta P(\mu_e) = P(\mu_e) - P_L(\mu_e)$, corresponding to the model in (a) resp. (c). Solid curves in (b) and (d) indicate boundaries of regions in exit angle space, numbered with the band index, for which coupling to a photonic single crystal is possible. Bands 2 and 4 are nearly polarization degenerate with bands 1 resp. 3, and similar to within the line thickness. In panels (e) and (f) predictions are shown for the photon exit distribution for an inverse opal $\varepsilon = 11.9$ cut along a 100 plane (instead of a 111 plane, as in panels (b,d)). The only allowed exit angles are in the white pockets, belonging to band 8 ($\omega a/2\pi c = 0.776$) for frequencies below the full band gap, panel (e), resp. band 9 ($\omega a/2\pi c = 0.816$ above the band gap, panel (f)).*

143

interpretation. In addition, the large angular extent of the internal reflection lines of strongly photonic crystals and the associated large enhancements cause a strongly non-Lambertian distribution of diffuse intensity over exit directions. In contrast, the angular distribution of photons for weakly photonic crystals is practically equal to the Lambertian distribution $P_L$ for angles outside the narrow internal reflection lines, since the extrapolation length is barely affected by internal reflection.

In a general analysis of the range of suppressed diffuse transmission at a specific frequency, it is necessary to determine the set of exit directions for which photons are blocked by internal reflection, *i.e.*, directions that do not couple to any Bloch mode. Such an analysis is outlined in Chapter 2.8, and is based on *(i)* photon dispersion surfaces in the photonic crystal, *(ii)* parallel momentum conservation at the interface, and *(iii)* causality requirements on the direction of the group velocity. We have determined dispersion surfaces and group velocities by interpolating from eigenfrequencies calculated on a dense k-grid within the volume of the irreducible wedge of the first Brillouin zone, and on the facets of the Brillouin zone[2]. In Figure 7.8(b),(d) the solid lines show results of solving the refraction problem for the two frequencies corresponding to the data. For clarity, only the *boundaries* of the forbidden regions in exit-angle space are indicated. For the frequency in the L-gap ($\omega = 8200$ cm$^{-1}$, Fig. 7.8(b)) coupling is only allowed to band 1 and the nearly polarization degenerate band 2, and is limited to $\alpha > 33°$, in perfect agreement with the data. For a higher frequency[3] above the L-gap ($\omega = 9300$ cm$^{-1}$, Fig. 7.8(d)) coupling to bands 1 and 2 is only allowed in 6 small lobes in exit angle space. For angles $\alpha < 34.5°$ coupling occurs to bands 3 and 4. For larger angles $\alpha > 51°$, 6 parabolas delimit angular ranges in which coupling from band 3 and 4 to air is allowed. The only angles to which diffuse light inside the samples can not couple are contained in a ring concentric with the origin, and 6 patches with $80° < \alpha < 90°$ and azimuthal width $\lesssim 6°$, too small to affect the experimental azimuthal average. The boundaries of the ring are sixfold symmetric, but not circular. Overall, the agreement of the central forbidden ring with the experimental data is gratifying.

Interesting possibilities are offered at frequencies near photonic band gap edges. For frequencies near the edge of any photonic band gap that closes away from the center of the Brillouin zone, all modes have wave vectors in pockets away from the k-space origin. In such cases, diffuse light may exit the photonic crystal only along isolated directions. As the shape of dispersion surfaces for frequencies near a band gap is nearly ellipsoidal, an effective mass approximation is well suited to predict the directionality of diffuse transmission. As an example which may soon be realized, we consider an inverse opal with a full photonic band gap, assuming a $\varepsilon = 11.9$ backbone containing *fcc* close-packed air spheres. In Figure 7.8(e) the solution of the refraction problem for a 100 cleaved crystal [35] is shown for a frequency $\hat{\omega} = \omega a/2\pi c$ just below the band gap. In the frequency range from $\hat{\omega} = 0.748$ up to the band gap edge $\hat{\omega} = 0.778$, the only allowed modes are in band 8, and the dispersion surfaces are ellipsoids

---

[2] We used 2992 equidistant k-points within the irreducible part of the Brillouin zone, 1816 points on the 111 facet and 1255 on the 200 facet of the Brillouin zone.

[3] Deeper analysis of the refraction problem is contained in Section 2.8 and Fig. 2.8.

around the W point. Diffuse light inside the crystal can only couple into a symmetric quadruplet of beams, with exit angles $\alpha$ relative to the sample normal around 40°. For frequencies *above* the band gap (limited by band 9 at the X-point) emission is directed into a central beam along the surface normal, with a width proportional to the square root of the detuning from the gap edge. Internal reflection causes the four beams at grazing exit angle (Fig. 7.8(f)) not to appear in a small frequency range just above the gap edge. In this frequency range, all light inside the crystal, be it multiply scattered from an external source or emission from inside the crystal, may only leave the crystal in one single narrow beam of diffuse light. Directional diffuse beams will occur for all band gap crystals for which the gap closes away from the k-space origin, including diamond, *fcc*, *hcp* and *bcc* structures.

## 7.7 Extrapolation length and total transmission

In this section we return to the experimental data of diffuse transmission of titania inverse opals. We use the extrapolation length ratio that results from the fit to the measured escape function to interpret the total transmission $T_{\omega,\gamma}$ of the titania inverse opals in terms of their transport mean free path. First, we present total diffuse-transmission measurements in Subsection 7.7.1. In Subsection 7.7.2 we analyze the frequency dependence of the extrapolation length ratio, and discuss total transmission corrected for internal reflections.

### 7.7.1 Total transmission

The total transmission of a sample with $a = 930$ nm as a function of frequency is shown in Figure 7.9(a) for incidence angles $\gamma = 0°$, 15° and 30°. The most apparent features are *(i)* a decrease of the total transmission with increasing frequency visible in all three traces and *(ii)* the occurrence of a band of reduced total transmission which shifts from 8100 cm$^{-1}$ to higher frequencies with increasing angle of incidence $\gamma$. The center frequency of the angle-dependent band of reduced total transmission coincides with the photonic stop band measured in a reflectivity measurement and with the stop band in the escape function. The center frequency of the stop band is inversely proportional to the lattice parameter, as demonstrated by the blue shifted spectrum for a sample with $a = 800$ nm in Fig. 7.9(a). As less light enters the sample for wave vectors matching the Bragg reflection condition, the diffuse intensity injected into the sample is reduced in a frequency region matching the stop band for the incident direction. This reduction of the total transmission is caused by the reflectivity of the front surface, the factor $[1 - R^{\text{front}}_{\omega,\gamma}]$ in Eq. (7.2). The stop band width in the total transmission measurement is larger than the photonic width due to the large angular width $\Delta\gamma \sim 10°$ of the incident beam. The stop band depth in total transmission is limited by the external reflectivity $R^{\text{front}}$, which amounts to 50 to 70% for a wide beam spanning many domains. The stop gap minimum of 0.09 at $\gamma = 0°$ in the total transmission is indeed only 2 to 3 times less than the value just outside the stop gap
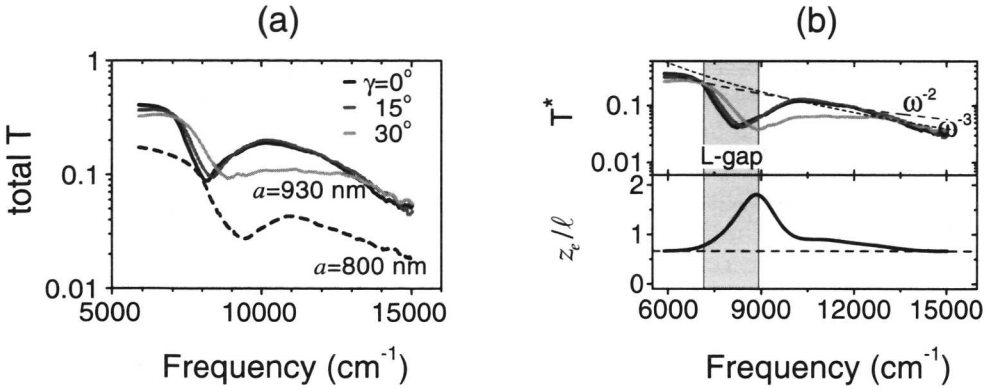
FIGURE 7.9: (a) Measured total diffuse transmission as a function of optical frequency for a sample with lattice parameter $a = 930$ nm for incidence angles $\gamma = 0°$, $15°$, $30°$ (solid lines, black, gray, light gray). For a sample with $a = 800$ nm the stop band at $\gamma = 0°$ (L-gap) is shifted to higher frequency (data indicated by the dashed line). Lower panel in (b): extrapolation length ratio $\tau_e = z_e/\ell$ pertaining to the fit to the data in Fig. 7.6. Upper panel in (b): $T^* = T/(1 + \tau_e[1 - 2T])$ versus $\omega$, i.e., total transmission data $T$ in (a) corrected for the frequency-dependent extrapolation length (model, lower panel) for incidence angles $\gamma = 0°, 15°, 30°$ (black, dark gray and light gray curves). Dashed lines represent the power laws $\omega^{-3}$ (short dashes), and $\omega^{-2}$ (long dashes).

of roughly 0.3. This should be contrasted to the typical attenuation of several decades for stop gaps in characteristic 'coherent transmission' measurements, in which the intensity transmitted along the direction of the incident beam is monitored. As the coherent transmission decays exponentially with $\ell_\omega/L$ such measurements are only feasible in thin (i.e., small $L$ [36]) or near-index matched (i.e., large $\ell$ [12]) photonic crystals. The stop gap in coherent transmission is determined by diffraction from all the differently oriented crystallites encountered along the trajectory of the forward beam. The cumulative effect of all crystallites in the bulk causes a stop gap with high attenuation, and a width larger than the intrinsic photonic width [23]. This broadening of the stop gap in coherent transmission is not only limited by the angular spread of the incident beam, however, but mainly caused by misaligned and strained crystallites [11].

The decrease of the total transmission with increasing frequency is caused by a decrease of the mean free path $\ell_\omega$ due to increasing scattering strength of defects at larger frequencies. We recognize two regimes in the total transmission, depending on the magnitude of the mean free path. Below $\omega = 7200$ cm$^{-1}$ the total transmission of $T \sim 0.3$ indicates that the sample thickness $L \sim 200$ $\mu$m is at most a few transport mean free paths ($\ell_\omega \approx 60$ $\mu$m). In this regime the sample is not truly multiple scattering, causing deviations from the diffusion law Eq. (7.2) which relates $\ell_\omega$ to the total transmission. For higher frequencies, we find a steeper decrease of the total transmission to $\sim 0.05$ at $\omega = 15000$ cm$^{-1}$, typical of $\ell_\omega \approx 10$ $\mu$m. As the thickness $L$ of

the samples is not well known, accurate values for the mean free path $\ell$ can not be extracted. Though the values $\ell = 10$ to $60\ \mu$m agree with enhanced backscattering experiments on other samples, we focus only on the scaling of $T$ with frequency. In the frequency range $\omega \geq 7200\ \text{cm}^{-1}$, the mean free path is sufficiently small compared to the sample thickness to expect the Ohmic diffuse-transmission law Eq. (7.2) to hold. As the lowest Bragg diffraction overlaps with this frequency range, the analysis of total transmission in terms of the mean free path is complicated by the frequency dependence of the extrapolation length ratio.

### 7.7.2 Extrapolation length ratio and scattering strength

In Figure 7.9(b) the extrapolation length ratio $\tau_{e,\omega} = z_{e,\omega}/\ell_\omega$ pertaining to the fit to the data in Fig. 7.6 is presented as a function of frequency. In the small frequency limit, the extrapolation length ratio equals 2/3, as there are no internal reflections[4]. As the optical frequency reaches the L-gap, the extrapolation length ratio grows to a maximum of nearly 1.8, corresponding to a maximum average internal-reflection coefficient $\bar{R}_\omega^D \sim 45\%$. This maximum is reached at the blue edge of the L-gap, where the largest fraction of solid angle is covered by stop gaps [26]. The avoided crossing of two stop bands at $\alpha \geq 30°$ enlarges the angle-averaged internal reflection in the same frequency window. For higher frequencies $\omega > 9500\ \text{cm}^{-1}$, the extrapolation length ratio diminishes, as the range of internally reflected angles decreases. Though the qualitative behavior of the extrapolation length ratio may be explained by the band structure, the numerical value of the maximum, and details of the functional dependence are determined by, $e.g.$, the depth of the stop gaps involved.

From Eq. (7.2) it is clear that for frequencies $outside$ a stop gap for the incident direction $\gamma$, for which $R_{\omega,\gamma}^{\text{front}} = 0$, the inverse optical thickness $\ell_\omega/L$ may be expressed in terms of $T_\omega$ and $\tau_{e,\omega}$ as

$$\frac{\ell_\omega}{L} = T_\omega^* := \frac{T_\omega}{1 + \tau_{e,\omega} - 2\tau_{e,\omega}T_\omega}. \tag{7.19}$$

Using the extrapolation length ratio $\tau_{e,\omega}$ plotted in Fig. 7.9(b), we extract $T_\omega^*$ from the total transmission spectra presented in Fig. 7.9(a). We proceed to discuss the scaling behavior of the decrease of $T_\omega^*$ with increasing frequency. As $T_\omega^*$ equals $\ell_\omega/L$ for frequencies outside a stop gap in total transmission, one might expect a $\omega^{-4}$ law typical for the scattering strength of particles much smaller than the wavelength, as reported for opals by Vlasov and coworkers [12]. Enhanced backscattering experiments on opals presented in Chapter 6, however, point at a scattering mechanism dominated by polydispersity and displacements. As scattering essentially occurs off thin 'difference' shells with size comparable to the wavelength, the associated scaling of the mean free path reaches into the quadratic Rayleigh-Gans regime for frequencies of the order of and above the lowest order Bragg diffraction. In this experiment, we find a decrease of $\ell_\omega/L$ which appears faster than $\omega^{-2}$ and slower than $\omega^{-3}$ (dashed lines in

---

[4]The Fresnel reflection due to the effective refractive index is neglected in this analysis.

Fig. 7.9(b)). This observation holds for all the samples with $a = 930, 900$ and $800$ nm, and was reproduced on samples with much smaller lattice parameters $a = 690$ and $500$ nm. The latter samples are optically thicker, and the probe frequencies in the range of the experiment remain below the L-gap, *i.e.*, in the long wavelength regime. Though the frequency dependence of $\ell$ remains partly obscured due to the stop gaps in total transmission, the scattering does not increase as fast as Rayleigh's $\omega^4$ law predicts. This is consistent with the scattering mechanism proposed in Chapter 6. One should bear in mind that the frequencies below and in the L-gap may belong to the cross-over regime from Rayleigh's $\omega^{-4}$ to Rayleigh-Gans's $\omega^{-2}$ scaling, in contrast to the higher frequencies used in Chapter 6. This may explain why $\ell$ decreases with frequency faster than $\omega^{-2}$ and slower than $\omega^{-3}$. The fabrication of periodic structures with template-assisted self-assembly [6, 35, 37–39]), lithographic [7, 8] and layer-by-layer microfabrication methods [9] all involve displacements, roughness and polydispersity of the same magnitude. Hence we expect the random scattering in all the current state of the art photonic structures to be comparable.

## 7.8 Conclusion

We have presented frequency-resolved measurements of the angular distribution of diffuse transmitted light from strongly photonic crystals. We find a drastic frequency-dependent angular redistribution of diffuse transmitted light due to internal Bragg reflection. Though the ranges of strong internal reflection are governed by gaps in the dispersion relation, it is imperative for accurate modelling to take the redistribution into angles not contained in a stop gap into account. The relevant parameter, *i.e.*, the extrapolation length ratio, can not be derived from the band structure, but requires a diffusion model. We have presented the first model combining diffusion and the photonic internal reflection due to the band structure. The extrapolation length ratio which we calculate has a broader relevance in interpreting standard experiments such as enhanced backscattering or total transmission aimed at determining the transport mean free path in the frequency range of photonic stop gaps. Application to the total transmission of strongly photonic crystals reveals a mean free path decreasing from $\sim 60$ to $\sim 10 \, \mu$m as the frequency increases from below the first stop gap to just below the second order Bragg reflection. This decrease is surprisingly slower than $\omega^{-4}$, indicating that polydispersity, roughness and site displacements of photonic building blocks form the dominant scattering mechanism.

The data and model presented here are especially relevant for the interpretation of emission measurements (see Chapters 3 and 4). The mechanism causing the angular dependence in emission spectra is the same diffuse internal reflection quantified here. Inspection of the stop bands in emission (Figure 3.2) show similar stop gap width, dispersion and depth as revealed by the escape function. Enhancement due to the extrapolation length may even be discerned in Figure 3.2(b). The internal reflectivity of the samples studied in this chapter (maximum $\sim 80\%$ for $\alpha = 0°$) is somewhat higher than the stop gap depth $\sim 50$ to $70\%$ quoted in Chapter 3. We therefore

expect the extrapolation length ratio to be $\sim 1.35\ell$ (*i.e.* $\bar{R}_{\omega}^{D} = 34\%$) in the emission experiments. This is consistent with the estimate in Chapter 4. In Chapters 3 and 4 the angular dependence was separated from the angle integrated emission power spectra based on prior knowledge of external reflectivity experiments. Especially the fact that exit angles occur for which no stop gap overlaps the emission spectrum was instrumental in the analysis. Furthermore the spontaneous emission inhibition could only be estimated from the data to within the limits set by the magnitude of the extrapolation length ratio. Escape function measurements using externally injected light are useful to separate the angular dependence of emission spectra from the angle-integrated emission without prior knowledge of the dispersion. We expect that spectrally resolved emission measurements in the range of second order Bragg diffraction will require such complementary escape function measurements. In this frequency range (near bands 8 and 9), a multitude of reflectivity bands that barely shift with angle occur [30], causing a concomitant complicated frequency dependence of the extrapolation length ratio.

Finally, we would like to point out the similarity between the general analysis of the angle-resolved diffuse intensity distribution in Section 7.6 and high-resolution angle-resolved photoemission spectroscopy. This powerful technique is instrumental in the study of surface and projected bulk electronic band structures and Fermi surfaces in, *e.g.*, metals or high $T_c$ superconductors [40, 41]. With this technique, the electron 'dispersion' surface (isoenergy surface) at the Fermi level translates into a structured angular distribution of photoelectrons. The analogy holds if the optical probe frequency is identified with the Fermi energy of the electron. Moreover, the optical experiment should be considered a zero temperature analogon of the electronic case. Experimentally, the probe depth in the photonic crystals, $\ell \lesssim 10$ unit cells, appears less restricted to the surface than in photoemission. Angle-resolved diffuse transmission on single crystal photonic crystals may prove to be a powerful technique for studying photonic dispersion. Theoretical analysis beyond the refraction construction (Fig. 7.8) may certainly benefit from electron theory developed for photoemission spectroscopy.

# References

[1] *Photonic Band Gap Materials*, edited by C. M. Soukoulis (Kluwer, Dordrecht, 1996).

[2] *Photonic Crystals and Light Localization in the 21$^{st}$ Century*, edited by C. M. Soukoulis (Kluwer, Dordrecht, 2001).

[3] Z.-Y. Li and Z. Q. Zhang, *Fragility of Photonic Band Gaps in Inverse-Opal Photonic Crystals*, Phys. Rev. B **62**, 1516 (2000).

[4] Z.-Y. Li, X. D. Zhang, and Z. Q. Zhang, *Disordered Photonic Crystals Understood by a Perturbation Formalism*, Phys. Rev. B **61**, 15738 (2000).

[5] J. S. Kole, *New Methods for the Numerical Solution of Maxwell's Equations*, Ph.D. thesis, Rijksuniversiteit Groningen, 2003.

[6] J. E. G. J. Wijnhoven, L. Bechger, and W. L. Vos, *Fabrication and Characterization of Large Macroporous Photonic Crystals in Titania*, Chem. Mater. **13**, 4486 (2001).

[7] T. Baba and N. Fukaya, *Light Propagation Characteristics of Defect Waveguides in a Photonic Crystal Slab*, in [2] 105 (2000).

[8] M. Notomi, K. Yamada, A. Shinya, J. Takahashi, C. Takahashi, and I. Yokohama, *Extremely Large Group-Velocity Dispersion of Line Defect Waveguides in Photonic Crystal Slabs*, Phys. Rev. Lett. **87**, 253902 (2001).

[9] S. Ogawa, K. Tomoda, and S. Noda, *Effects of Structural Fluctuations on Three-Dimensional Photonic Crystals Operating at Near Infrared Wavelengths*, J. Appl. Phys. **91**, 513 (2002).

[10] J. Galisteo Lòpez and W. L. Vos, *Angle Resolved Reflectivity of Single-Domain Photonic Crystals, Effects of Disorder*, Phys. Rev. E **66**, 036616 (2002).

[11] W. L. Vos, M. Megens, C. M. van Kats, and P. Bösecke, *Transmission and Diffraction by Photonic Colloidal Crystals*, J. Phys.-Condens. Matter **8**, 9503 (1996).

[12] Y. A. Vlasov, M. A. Kaliteevski, and V. V. Nikolaev, *Different Regimes of Light Localization in a Disordered Photonic Crystal*, Phys. Rev. B **60**, 1555 (1999).

[13] A. F. Koenderink, M. Megens, G. van Soest, W. L. Vos, and A. Lagendijk, *Enhanced Backscattering from Photonic Crystals*, Phys. Lett. A **268**, 104 (2000).

[14] J. Huang, N. Eradat, M. E. Raikh, Z. V. Vardeny, A. A. Zakhidov, and R. H. Baughman, *Anomalous Coherent Backscattering of Light from Opal Photonic Crystals*, Phys. Rev. Lett. **86**, 4815 (2001).

[15] A. Ishimaru, *Wave Propagation and Scattering in Random Media* (Academic Press, New York, 1978).

[16] P. Sheng, *Introduction to Wave Scattering, Localization, and Mesoscopic Phenomena* (Academic Press, New York, 1995).

[17] A. Lagendijk, R. Vreeker, and P. de Vries, *Influence of Internal Reflection on Diffusive Transport in Strongly Scattering Media*, Phys. Lett. A **136**, 81 (1989).

[18] J. X. Zhu, D. J. Pine, and D. A. Weitz, *Internal Reflection of Diffusive Light in Random Media*, Phys. Rev. A **44**, 3948 (1991).

[19] M. U. Vera and D. J. Durian, *Angular Distribution of Diffusely Transmitted Light*, Phys. Rev. E **53**, 3215 (1996).

[20] J. Gómez Rivas, R. Sprik, A. Lagendijk, L. D. Noordam, and C. W. Rella, *Mid-Infrared Scattering and Absorption in Ge Powder Close to the Anderson Localization Transition*, Phys. Rev. E **62**, R4540 (2000).

[21] J. Gómez Rivas, R. Sprik, A. Lagendijk, L. D. Noordam, and C. W. Rella, *Static and Dynamic Transport of Light Close to the Anderson Localization Transition*, Phys. Rev. E **63**, 046613 (2001).

[22] F. J. P. Schuurmans, D. Vanmaekelbergh, J. van de Lagemaat, and A. Lagendijk, *Strongly Photonic Macroporous Gallium Phosphide Networks*, Science **284**, 141 (1999).

[23] M. Megens, J. E. G. J. Wijnhoven, A. Lagendijk, and W. L. Vos, *Light Sources Inside Photonic Crystals*, J. Opt. Soc. Am. B **16**, 1403 (1999).

[24] H. P. Schriemer, H. M. van Driel, A. F. Koenderink, and W. L. Vos, *Modified Spontaneous Emission Spectra of Laser Dye in Inverse Opal Photonic Crystals*, Phys. Rev. A **63**, 011801 (2001).

[25] M. Notomi, *Theory of Light Propagation in Strongly Modulated Photonic Crystals: Refractionlike Behavior in the Vicinity of the Photonic Band Gap*, Phys. Rev. B **62**, 10696 (2000).

[26] M. S. Thijssen, R. Sprik, J. E. G. J. Wijnhoven, M. Megens, T. Narayanan, A. Lagendijk, and W. L. Vos, *Inhibited Light Propagation and Broadband Reflection in Photonic Air-Sphere Crystals*, Phys. Rev. Lett. **83**, 2730 (1999).

[27] H. M. van Driel and W. L. Vos, *Multiple Bragg Wave Coupling in Photonic Band-Gap Crystals*, Phys. Rev. B **62**, 9872 (2000).

[28] S. G. Romanov, T. Maka, C. M. S. Torres, M. Müller, R. Zentel, D. Cassagne, J. Manzanares-Martinez, and C. Jouanin, *Diffraction of Light from Thin-Film Polymethylmethacrylate Opaline Photonic Crystals*, Phys. Rev. E **63**, 056603 (2001).

[29] D. J. Durian, *Influence of Boundary Reflection and Refraction on Diffusive Photon Transport*, Phys. Rev. E **50**, 857 (1994).

[30] W. L. Vos and H. M. van Driel, *Higher Order Bragg Diffraction by Strongly Photonic Fcc Crystals: Onset of a Photonic Bandgap*, Phys. Lett. A **272**, 101 (2000).

[31] T. Yoshiyama and I. Sogami, *Kossel Line Analysis on Colloidal Crystals in Semidilute Aqueous Solutions*, Phys. Rev. Lett. **53**, 2153 (1984).

[32] İ. İ. Tarhan and G. H. Watson, *Photonic Band Structure of Fcc Colloidal Crystals*, Phys. Rev. Lett. **76**, 315 (1996).

[33] W. Kossel, V. Loeck, and H. Voges, *Die Richtigungsverteilung der in einem Kristall enstandenen charakteristischen Röntgenstrahlung*, Z. f. Physik **94**, 139 (1935).

[34] R. W. James, *The Optical Principles of the Diffraction of X-Rays* (G. Bell & Sons, London, 1954).

[35] Y. A. Vlasov, X. Z. Bo, J. C. Sturm, and D. J. Norris, *On-Chip Natural Assembly of Silicon Photonic Bandgap Crystals*, Nature **414**, 289 (2001).

[36] J. F. Bertone, P. Jiang, K. S. Hwang, D. M. Mittleman, and V. L. Colvin, *Thickness Dependence of the Optical Properties of Ordered Silica-Air and Air-Polymer Photonic Crystals*, Phys. Rev. Lett. **83**, 300 (1999).

[37] J. E. G. J. Wijnhoven and W. L. Vos, *Preparation of Photonic Crystals Made of Air Spheres in Titania*, Science **281**, 802 (1998).

[38] A. Blanco, E. Chomski, S. Grabtchak, M. Ibisate, S. John, S. W. Leonard, C. López, F. Meseguer, H. Míguez, J. P. Mondia, G. A. Ozin, O. Toader, and H. M. van Driel, *Large-Scale Synthesis of a Silicon Photonic Crystal with a Complete Three-Dimensional Bandgap Near 1.5 Micrometres*, Nature **405**, 437 (2000).

[39] O. D. Velev and E. W. Kaler, *Structured Porous Materials Via Colloidal Crystal Templating: From Inorganic Oxides to Metals*, Adv. Mater. **12**, 531 (2000).

[40] S. Hüfner, *Photoelectron Spectroscopy: Principles and Applications* (Springer Verlag, Berlin, 1995), and references therein.

[41] S. V. Borisenko, M. S. Golden, S. Legner, T. Pichler, C. Durr, M. Knupfer, J. Fink, G. Yang, S. Abell, and H. Berger, *Joys and Pitfalls of Fermi Surface Mapping in $Bi_2Sr_2CaCu_2O_{8+\delta}$ Using Angle Resolved Photoemission*, Phys. Rev. Lett. **84**, 4453 (2000).